The Journal of Chemical Physics

RESEARCH ARTICLE | JUNE 30 2025

Characterization of the hemithioindigo photoswitch and its derivatives with x-ray photoabsorption and photoemission spectroscopies

L. Oberti ; L. Avaldi ; P. Bolognesi ; M. Bonanomi; R. Borrego-Varillas ; C. Callegari ; L. Carlini; J. Chiarinelli ; E. Ciekalski ; M. Coreno ; M. Devetta ; M. Di Fraia ; M. Garavelli ; M. Goffe ; C. Grazioli ; F. Montorsi; K. C. Prince ; R. Richter ; F. Segatta ; S. Waldmannstetter; G. Cerullo ; H. Dube ; O. Plekan ; D. Faccialà ; C. Vozzi ; A. Nenov

J. Chem. Phys. 162, 244202 (2025)
https://doi.org/10.1063/5.0271164
CHORUS

The Journal of Chemical Physics ARTICLE pubs.aip.org/aip/jcp

Characterization of the hemithioindigo photoswitch and its derivatives with x-ray photoabsorption and photoemission spectroscopies

Cite as: J. Chem. Phys. 162, 244202 (2025); doi: 10.1063/5.0271164
Submitted: 15 March 2025 • Accepted: 5 June 2025 •
Published Online: 30 June 2025

L. Oberti,[1,2,3] L. Avaldi,[4] P. Bolognesi,[4] M. Bonanomi,[1,2] R. Borrego-Varillas,[2] C. Callegari,[5] L. Carlini,[4] J. Chiarinelli,[4] E. Ciekalski,[6] M. Coreno,[5,7] M. Devetta,[2] M. Di Fraia,[5] M. Garavelli,[8] M. Goffe,[8] C. Grazioli,[5,9] F. Montorsi,[8] K. C. Prince,[5,10] R. Richter,[5,a)] F. Segatta,[8] S. Waldmannstetter,[6] G. Cerullo,[1,2] H. Dube,[6] O. Plekan,[5] D. Facciala,[2,b)] C. Vozzi,[2,b)] and A. Nenov[8,b)]

AFFILIATIONS

[1]Politecnico di Milano, Physics Department, Piazza Leonardo da Vinci 32, 20133 Milan, Italy
[2]CNR, Istituto di Fotonica e Nanotecnologie, Piazza Leonardo da Vinci 32, 20133 Milan, Italy
[3]Deutsches Elektronen Synchrotron (DESY), 22607 Hamburg, Germany
[4]CNR, Istituto di Struttura della Materia, Sede Secondaria di Montelibretti, Area della Ricerca di Roma 1, Monterotondo Scalo, Italy
[5]Elettra-Sincrotrone Trieste, Strada Statale 14—km 163.5, in AREA Science Park, IT-34149 Basovizza, Trieste, Italy
[6]Friedrich-Alexander-Universität Erlangen-Nürnberg Department of Chemistry and Pharmacy, Nikolaus-Fiebiger-Str. 10, 91058 Erlangen, Germany
[7]ISM-CNR, Instituto di Struttura della Materia, LD2 Unit, 34149 Trieste, Italy
[8]Università di Bologna—Alma Mater Studiorum, Dipartimento di Chimica Industriale "Toso Montanari," Via Piero Gobetti 85, 40129 Bologna, Italy
[9]IOM-CNR, Istituto Officina dei Materiali, Basovizza SS-14, Km 163.5, 34149 Trieste, Italy
[10]Charles University, Faculty of Mathematics and Physics, Department of Surface and Plasma Science, V Holešovičkách 2, Prague 18000, Czech Republic

[a)]Deceased.
[b)]**Authors to whom correspondence should be addressed:** artur.nenov@unibo.it; davide.facciala@cnr.it; and caterina.vozzi@ifn.cnr.it

ABSTRACT

In this study, we investigate the electronic structure of hemithioindigo–hemistilbene (HTI) photoswitches and their functionalized derivatives, HTI-OMe and HTI-SMe, using x-ray photoemission spectroscopy (XPS) and near-edge x-ray absorption fine structure (NEXAFS) spectroscopy. HTI compounds are known for their high quantum yield, thermal bistability, and rapid photoisomerization, making them promising candidates for applications in molecular motors, optical materials, and photocatalysis. Our analysis, supported by first-principles simulations, reveals how the conjugation of heteroatoms within the π-system affects the core-level chemical shifts and ionization intensities in XPS, while NEXAFS probes the influence of substituents on virtual molecular orbitals and energy transitions. In particular, the comparison between different functionalized HTIs allowed us to evaluate the effect of electronic relaxation following core-level photoionization and photo-excitation. These results provide a detailed understanding of the influence of functionalization on the electron distribution of HTI compounds, providing a robust foundation for the study and control of ultrafast charge transfer and photoswitching mechanisms in these molecular systems.

I. INTRODUCTION

Photoswitches are molecules that can change between two (or more) isomeric forms after photoexcitation. This quality makes them interesting for a wide range of technological applications in the fields of biology, chemistry, medicine, photocatalysis, and optics. Hemithioindigo–hemistilbene (HTI) dyes are a class of photoswitches that exhibit E–Z double bond isomerization when exposed to visible or ultraviolet light. HTI consists of a thioindigo and a stilbene fragment connected through a central double bond. The Z isomeric form is thermodynamically stable and can be photoisomerized to the metastable E isomeric form. The uniqueness of HTI switches relies on their high quantum yields, their responsiveness to the visible part of the electromagnetic spectrum, and their high thermal bistability, compared to other common photoswitches.[1] Owing to these properties, HTI molecules can be used as molecular motors,[2–5] ultrafast molecular switches in biological chromopeptides[6] for new optical materials, or as a control unit of three-dimensional peptide structures[7] and their related biological functions. For example, they play a role in the development of innovative optical materials, the advancement of supramolecular chemistry,[8] and the ability to perform light-controlled catalysis.[9] HTI molecules serve as components in molecular threading machines[10] and act as molecular photogears.[11] These versatile molecules have also provided insights into exotic photoreactions such as the hula-twist mechanism, along with the discovery of novel dual-single-bond rotations.[12–14] The kinetics of photoisomerization in unmodified HTIs occur within the picosecond temporal range. In particular, the Z isomer of the parent compound has an excited state lifetime of 38 ps. It has been experimentally demonstrated that an increase in the photoisomerization rate can be achieved by acting on external parameters[15] such as the solvent viscosity or polarity[16,17] or through internal parameters such as functionalization. Studies using transient UV/Vis spectroscopy have revealed that HTI-OMe and HTI-SMe, bearing a methoxy group (OMe) and a thiomethyl group (SMe), respectively (see Fig. 1), are among the fastest HTI derivatives, capable of isomerizing an order of magnitude faster (Z lifetime less than 5 ps[18]), highlighting the tremendous impact functionalization can have on the (photo)physics of a molecular system.

In particular, it has been predicted that the photoisomerization mechanism is driven by a significant charge polarization, creating, respectively, positive and negative charges on the phenyl and hemithioindigo moieties. The charge transfer configuration is strongly influenced by the nature of the substituents and their ability to modulate the electron density distribution within the molecular system.[18,19] In this context, the observed acceleration in the isomerization rate of HTI-OMe and HTI-SMe has been attributed to the ability of the strong donating groups to stabilize the positive charge on the phenyl, thus lowering the excited state isomerization barrier. In this framework, x-ray photoemission spectroscopy (XPS) and near-edge x-ray absorption fine structure (NEXAFS) spectroscopy represent the optimal probes to investigate, locally, how the electron density is affected by functionalization. These techniques, when applied to study the ground state of the molecule, not only provide an essential foundation for understanding photoexcitation dynamics but also offer direct access to detailed information on the electronic structure of HTI dyes in both the initial and final states of the photoionization/photoexcitation process. This allows for a precise investigation of how different substituents influence the chemical environment and how they affect the electronic relaxation following x-ray photon interaction.

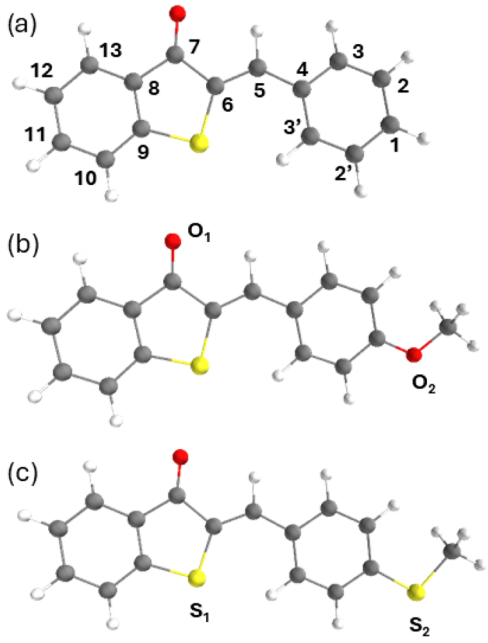

FIG. 1. Z isomer structure of molecules studied in this work labeled as HTI (a), HTI-OMe (b), and HTI-SMe (c).

In this work, we studied HTI and the two derivatives, HTI-OMe and HTI-SMe, by XPS and NEXAFS at the K-edges of carbon and oxygen, as well as at the $L_{2,3}$ edge of sulfur, accompanied by advanced simulations from first principles using the restricted active space self-consistent field (RASSCF) method corrected by multi-reference second-order perturbation theory (RASPT2).[20] This comparative study allowed us to elucidate the effect of the chemical environment and electronic relaxation on the chemical shifts and intensities of specific atomic sites, as well as to rationalize differences in the signatures of specific donors on the photoswitch electronic structure. In particular, XPS allowed us to reveal how both the intensity and the chemical shift of the core ionization signal from the ground state of the molecule are strongly dependent on the degree of conjugation of the substituent heteroatom in the π-system of the aromatic ring. NEXAFS builds on this by probing vacant molecular orbitals, showing how the inductive and mesomeric strength of the functional groups affects the shape of the molecular orbitals and, consequently, the brightness of the transitions.

The observed physics points to the intrinsic properties of the functional groups. These properties provide essential insights into the electron distribution in the excited state, laying the groundwork for understanding and controlling the photoswitching mechanisms.

II. EXPERIMENTAL AND THEORETICAL METHODS

A. Experimental section

The photoelectron spectroscopy experiments were performed at the Gas-Phase Photoemission Beamline (GAPH) of the Elettra

synchrotron,[21] which provides tunable, monochromatic and linearly polarized radiation in the range of 13.5–900 eV. With its extensive energy span, exceptional resolving power, and high flux capabilities, combined with purpose-built end-stations, GAPH is an ideal platform for investigating the spectroscopy and dynamics of ionization phenomena, inner-shells, and multiple excitations. The end station was equipped with a VG-220i hemispherical deflection analyzer. The analyzer was operated in constant pass energy mode, in which the energy resolution is constant throughout the spectrum. Different pass energies were used for spectra recorded at the various edges. For HTI-OMe, a cold finger cooled by liquid nitrogen was included in the experimental chamber. This step was necessary to prevent overlap between the oxygen 1s peak of residual water and that of the oxygen of the functional group. The XPS spectra were measured at a photon energy of 382 eV for C(1s), 578 eV for O(1s), and 240 eV for S(2p). The NEXAFS photoabsorption spectra were acquired by measuring the total ion yield with a channel electron multiplier. The ion yields were measured at different photon energies across the C(1s), O(1s), and S(2p) near-edge regions and were normalized to the photon beam intensity measured by a photodiode placed at the end of the beamline. The XPS and NEXAFS spectra were calibrated using different reference gases. For the carbon and oxygen edges, CO_2 served as the reference, with the following binding energy and transition values: C(1s) at 297.7 eV, O(1s) at 541.3 eV, C(1s) $\rightarrow \pi^*$ at 290.77 eV, and O(1s) $\rightarrow \pi^*$ at 535.4 eV (Refs. 22–25). For the sulfur edge, SF_6 was used as the reference, with the following energy values: $S(2p_{3/2})$ at 180.2 eV and $S(2p_{1/2})$ at 181.5 eV, and $2p_{1/2} \rightarrow t_{2g}$ at 184.3 eV (Refs. 26–28).

Synthesis and purification of the Z isomers of each molecule were carried out by adapting published procedures.[18,29] To assess thermal stability, purity, and working conditions before the synchrotron experiments, Time-of-Flight (TOF) mass spectrometry preliminary tests were conducted on the first batch of molecules. The spectrometer and some of the procedures are described in Ref. 30. The preliminary mass spectra of the first batch revealed a small but non-negligible signal of precursor and solvent fragments. These contributions significantly decreased when the sample was kept stable at high temperatures (up to 120 °C) for several days. This suggests that pre-heating the substance is advisable for its purification. To confirm that heating at such high temperatures did not irreversibly degrade the sample, the IR spectra of the pristine sample and the one post-heating were compared (see the supplementary material, Chap. III). The IR spectra showed no differences that would indicate sample degradation. Based on these results, a new batch of molecules was synthesized with additional purification steps. The purified samples achieved a high purity of 99%, as measured by elemental analysis and NMR spectroscopy. Before starting the measurements, the new batch of molecules was preheated for 2 days at 60–70 °C in a crucible wrapped with a hot metal wire to remove any residual precursors or impurities. The preheated samples were then transferred to a custom-made oven terminating in a needle, designed to produce an effusive beam with a high density of the vapor sample in the interaction region. The effectiveness of the improved purification procedures was confirmed during the experiment by monitoring the valence photoelectron spectra (PES), collected at a photon energy of 92 eV. The PES indicated the complete absence of precursor and solvent-related signals, with only residual water initially present. After progressively heating the sample from 30 to ~70 °C over nine hours, the water signal in the PES disappeared. Under these conditions, the XPS and NEXAFS experiments were conducted, with the sample maintained at a stable temperature of ~70 °C.

B. Theoretical methods

The XPS and NEXAFS spectra are computed according to the following formulas:

$$\begin{aligned} \mathrm{I}^{\mathrm{XPS}}(\varepsilon) &= \sum_{\alpha} \sum_{i} Dy_{gi,\alpha} e^{-\frac{(\varepsilon - BE_{gi,\alpha})^2}{2\sigma^2}}, \\ \mathrm{I}^{\mathrm{NEXAFS}}(\varepsilon) &= \sum_{\alpha} \sum_{i} \mu^2_{gi,\alpha} e^{-\frac{(\varepsilon - \Delta\varepsilon_{gi,\alpha})^2}{2\sigma^2}}, \end{aligned} \tag{1}$$

where α iterates over all the atoms of a given type, $BE_{gi,\alpha}$ and $\Delta\varepsilon_{gi,\alpha}$ denote the binding and transition energies between the ground state g and the ith core-ionized/excited state, respectively, while $Dy_{gi,\alpha}$ and $\mu_{gi,\alpha}$ indicate the Dyson norm (i.e., pole strength) and the transition dipole moment $\mu_{gi,\alpha}$, respectively. σ denotes the empirical broadening, which originates from the convolution of the analyzer resolution, the spectral bandwidth of the synchrotron after the monochromator, and the width of the state. It has been adjusted to match the experiment, and it is assigned the same value for all transitions of a given atom type.

The protocol for obtaining the quantities required to simulate XPS and NEXAFS spectra has been presented and benchmarked previously[20,31] and is briefly outlined hereafter. All quantum chemical computations necessary for the simulations were performed using the quantum mechanics (QM) software OpenMolcas,[32] starting from MP2 optimized geometries. Scalar relativistic effects are taken into account through a decoupling of the relativistic Dirac Hamiltonian via the exact-two-component (X2C) approach[33] in combination with a relativistic atomic natural orbital basis set, ANO-R.[34] The electronic structure of the ground state and of the core-excited and core-ionized manifolds were obtained at the state averaged (SA)-RASSCF/single state (SS)-RASPT2 level of theory,[35,36] relying on an active space consisting of the core orbital(s) of a single atom placed in the sub-space RAS1 and kept frozen, and valence occupied and virtual orbitals, distributed between subspaces RAS2 and RAS3, respectively. The localized core orbitals are obtained by means of the Cholesky localization scheme.[37] Transitions from the core-orbitals are achieved within the core-valence separation (CVS) approximations by applying a projection technique to RAS1, which sets to zero the coefficients for those configuration state functions with a maximum occupation from a given subspace, thus effectively projecting these configurations out of the wave function.[38] Allowing simultaneous triple intra-valence excitations (i.e., from RAS2 to RAS3) enables the description of electron correlation and shake-up satellites. These are less intense features in the spectra arising from mixed double excitations in which a core-excitation is accompanied by a valence electronic transition. In the following, we will use the notation RAS(n, 1, 4; a, b, c), where the first three labels indicate the number of electrons in the active space, the maximum number of holes in RAS1, and the maximum number

of excitations in RAS3, while the last three labels denote the number of orbitals in the three sub-spaces.

Perturbation correction to the RASSCF solutions is added using the single-state flavor of RASPT2 with an imaginary shift of 0.2 a.u. and Ionization Potential Electron Affinity (IPEA) set to 0.0 a.u. The number of frozen orbitals was set to zero. Dyson norms[39] and transition dipole moments were calculated with the RAS state interaction routine (RASSI) module.[40] To facilitate this, in practice, the neutral ground electronic state has to be computed in a state-specific fashion (i.e., SS-CASSCF/SS-CASPT2) with an active space composition identical to the one used for the core calculations. The RASSI module was also used to compute spin–orbit coupling (SOC) terms, necessary to reproduce the relativistic effect at the sulfur $L_{2,3}$ edge. A density-fitting approximation, known as the Cholesky decomposition[41] of the electron repulsion integrals, was used to speed up the calculation of two-electron integrals. Sub-eV rigid shifts were applied to the spectra to maximize the overlap with the experimental spectra (values provided in the captions of the corresponding figures).

Edge-specific parameters adopted in this work are provided in the supplementary material, Chap. IV.

III. RESULTS AND DISCUSSION

A. XPS core-ionization spectra

1. Carbon 1s ionization

The carbon 1s experimental and theoretical XPS spectra for the three samples are shown in Fig. 2. In all figures, the total simulated spectrum, obtained by convoluting the signals of all carbon atoms, is shown with a dashed blue line, while contributions from individual atoms are indicated with colored sticks. Table I(a) lists the computed binding energies (BEs) for each carbon in HTI, while Tables I(b) and I(c) report the BEs only for those carbon atoms of HTI-OMe and HTI-SMe that show significant chemical shifts with respect to HTI, together with the BE of the carbon of the methoxy and thiomethyl groups.

The spectra of all three samples are dominated by a single band peaking around 290.4 eV, which strongly resembles the spectrum of benzothiophene reported by Toffoli *et al.*[42] The main peak is accompanied by a less intense band around 292.6 eV. The high energy part of the spectrum above 291 eV exhibits visible differences between the three species, such as the form of the shoulder of the main peak (at 291 eV) in the spectrum of HTI-SMe, the appearance of an additional band at 291.7 eV in the spectrum of HTI-OMe, and the increased intensity of the 292.6 eV band in the spectrum of HTI-OMe.

The calculations allow us to pinpoint the nature of the signals and to rationalize the differences. The main peak is formed by contributions from the majority of carbon atoms with nearly identical intensities. The shoulder at 291.0 eV and the band at 292.6 eV arise due to the ionization of C9 and C7, respectively. Notably, the BE of C7 has a particularly large chemical shift with respect to the main peak, of more than 2 eV. This is an effect that is observed also in the non-relaxed Koopmans' core-ionization energies (supplementary material, Table I), indicating that it originates from the distinct chemical environment present before photoionization, representing an *initial-state* effect. Indeed, the strongly electronegative oxygen in its proximity withdraws electron density from the C7 site, reducing the screening of the carbon 1s photoelectron.

Functionalization with methoxy and thiomethyl affects mainly the signatures of the hemistilbene moiety. The BE of the carbon

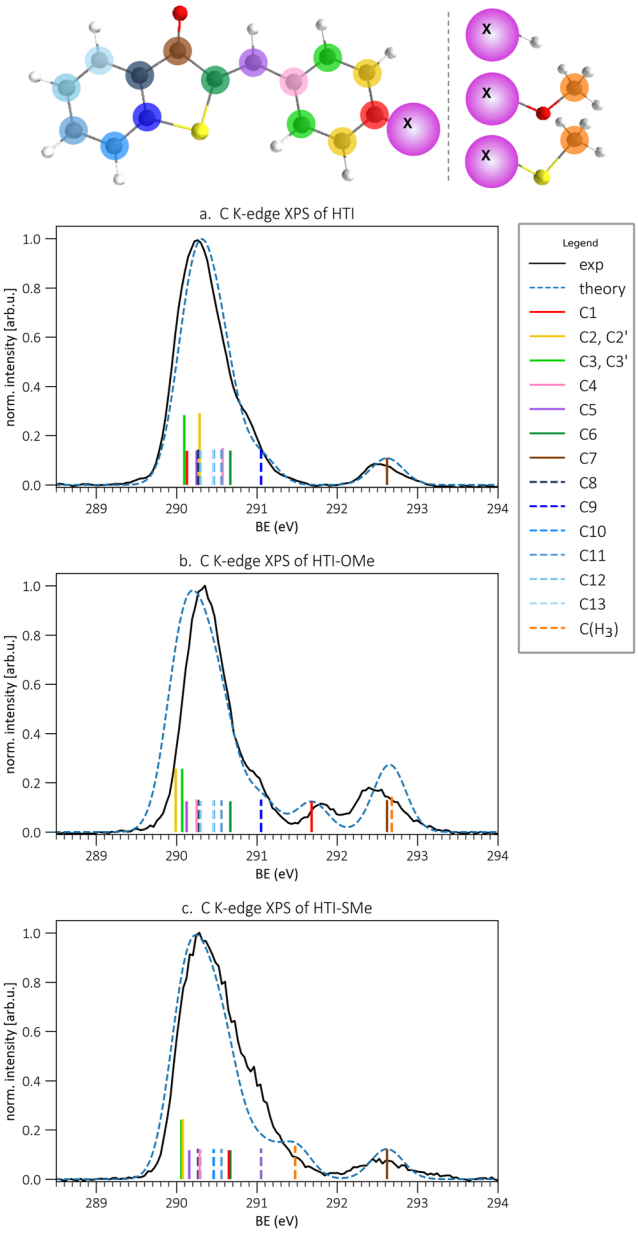

FIG. 2. Experimental (black line) and calculated (dashed line) carbon 1s XPS spectra of HTI (a), HTI-OMe (b), and HTI-SMe (c). The calculated spectra have been shifted by +0.35 eV to match the experiment. The sticks represent single-atom contributions. For the numbering of the C atoms, see Fig. 1, and for the color coding in the legend, see top of the figure.

TABLE I. Calculated binding energies (BEs) for HTI, HTI-OMe, and HTI-SMe at the carbon 1s edge. Table (a) lists the BEs for each carbon in HTI, while Tables (b) and (c) report the BEs only for those carbon atoms of HTI-OMe and HTI-SMe that show significant chemical shifts with respect to HTI (relative shift reported in boldface in parentheses), together with the BE of the carbon of the methoxy and thiomethyl groups. The BE values have been shifted by +0.35 eV in agreement with the plots in Fig. 2. For the numbering of the C atoms, see Fig. 1.

Carbon 1s edge

(a) HTI

Transition	BE (eV)	Dyson norm	Leading CSFs
C_1	290.13	0.62	C1(1s) ionization
$C_{2,2'}$	290.29	0.66 (x2)	C2(1s)/C2′(1s) ionization
$C_{3,3'}$	290.10	0.64 (x2)	C3(1s)/C3′(1s) ionization
C_4	290.57	0.67	C4(1s) ionization
C_5	290.25	0.62	C5(1s) ionization
C_6	290.67	0.62	C6(1s) ionization
C_7	292.62	0.65	C7(1s) ionization
C_8	290.27	0.65	C8(1s) ionization
C_9	291.05	0.66	C9(1s) ionization
C_{10}	290.46	0.64	C10(1s) ionization
C_{11}	290.56	0.65	C11(1s) ionization
C_{12}	290.30	0.63	C12(1s) ionization
C_{13}	290.46	0.65	C13(1s) ionization

(b) HTI-OMe

Transition	BE (eV)	Dyson norm	Leading CSFs
C_1	291.68 (**+1.55**)	0.62	C1(1s) ionization
$C_{2,2'}$	289.99 (**−0.30**)	0.64 (x2)	C2(1s)/C2′(1s) ionization
C_4	290.25 (**−0.32**)	0.66	C4(1s) ionization
$C(H_3)$	292.68	0.73	$C(H_3)$ (1s) ionization

(c) HTI-SMe

Transition	BE (eV)	Dyson norm	Leading CSFs
C_1	290.65 (**+0.52**)	0.62	C1(1s) ionization
$C_{2,2'}$	290.08 (**−0.21**)	0.64 (x2)	C2(1s)/C2′(1s) ionization
C_4	290.29 (**−0.28**)	0.65	C4(1s) ionization
$C(H_3)$	291.48	0.72	$C(H_3)$ (1s) ionization

ipso to the functional group (C1) displays a pronounced shift to higher energies corresponding to +1.55 eV for −OMe and +0.55 eV for −SMe compared to the HTI counterpart. In addition, in this case, the shift is similar to the one obtained from the non-relaxed BE values (supplementary material, Table I) and proportional to the electronegativity strength of the oxygen and sulfur relative to carbon, which points again to an initial-state effect. The strong shift experienced by C1 in HTI-OMe explains the additional band at 291.7 eV. In contrast, the BEs of the remaining atoms of the phenyl ring show a shift to lower energies. This is a manifestation of the positive mesomeric effect (+M) exerted by groups such as −OMe and −SMe, which donate electron density to the phenyl ring over the π-system and allow better shielding of the hole created upon ionization. The effect does not decay linearly with the distance from the functionalization site. C2, C2′, and C4 show a shift to lower energies of about 0.2–0.3 eV, while C3 and C3′ remain unaffected (a redshift of <0.05 eV).

Finally, the functional groups introduce a methyl carbon in the system linked directly to the heteroatom. The $-CH_3$ carbon peak coincides with the C7 peak in HTI-OMe at 292.6 eV, leading to the increased intensity of this feature. In HTI-SMe, the $-CH_3$ carbon peak contributes to the shoulder of the main band, thus explaining the subtle differences in line shapes. Notably, the BEs of the two

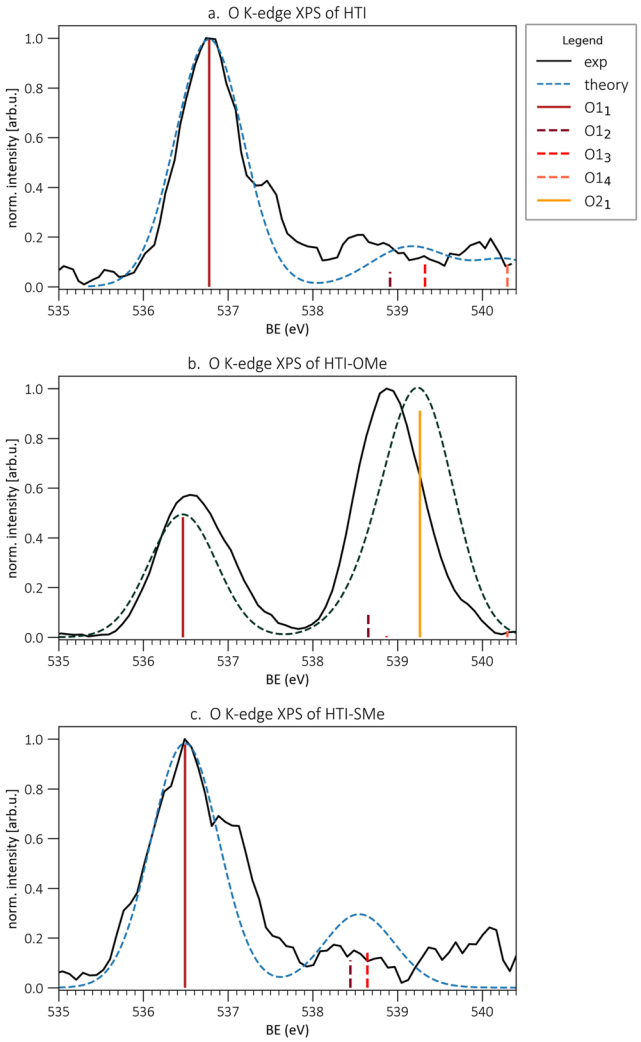

FIG. 3. Experimental (black line) and calculated (dashed line) oxygen 1s XPS spectra of HTI (a), HTI-OMe (b), and HTI-SMe (c). The calculated spectra have been shifted by +0.35 eV in order to match the experiment. In HTI-OMe, O1 and O2 refer to the carbonyl and methoxy oxygen atoms, respectively (see Fig. 1). The dashed vertical lines represent the shake-up energies.

carbon atoms *ipso* to the heteroatom of the functional group (C1 and CH_3) exhibit different BEs, with that of the methyl-carbon being ~1 eV blueshifted with respect to C1. This can be clearly observed in the experimental XPS spectrum of HTI-OMe, where the two contributions are well separated from the main peak. We note that the calculated non-relaxed BE values (Koopmans' core-ionization energies) of C1 and CH_3 differ by only 0.1 eV in both HTI-OMe and HTI-SMe (see the supplementary material, Table I). This indicates that the observed 1 eV blueshift of CH_3 with respect to C1 must originate from the different electronic density relaxation that follows the core-hole creation, which is referred to as a *final-state* effect. Indeed, since CH_3 does not participate in the aromatic system, its capability to withdraw electron density from the π-system upon ionization is strongly reduced compared to the atoms in the aromatic system (such as C1), which results in a lower screening of the core hole.

2. Oxygen 1s ionization

The experimental and theoretical oxygen K-edge XPS spectra of the three samples are shown in Fig. 3. Table II reports the computed BEs.

In all three spectra, we observe a common peak that exhibits a weak asymmetric broadening, a signature of the vibrational contributions to the line shape. This peak is assigned to the carbonyl oxygen ($O1_1$) and shifts from 536.6 to 536.4 eV upon functionalization with either −OMe or −SMe. For HTI and HTI-SMe, we notice a non-zero noisy signal at energies higher than 538 eV. In the spectrum of HTI-OMe, an additional peak appears at 539.0 eV, shifted by 2.3 eV with respect to the carbonyl oxygen, which can be tentatively assigned to the methoxy oxygen ($O2_1$). Remarkably, it is nearly twice as intense as the carbonyl oxygen peak.

For HTI and HTI-SMe, the signal at higher energies is assigned to shake-up satellites, whose calculated energy is shown by dashed lines in various tones of red. Nevertheless, a residual contribution from water around 540 eV cannot be excluded.[43] While shake-up features associated with O1 are also present in HTI-OMe in the region around 539.0 (dashed dark red line), their intensity is not sufficient to explain the twofold increase in intensity of the OMe oxygen peak.

Such a significant difference in intensities between the two oxygen 1s peaks is not common in gas-phase photoelectron spectroscopy experiments, where it is often assumed that the relative intensity reflects the stoichiometry.[44] In the case of HTI-OMe, quantitative analysis based on stoichiometry might suggest the presence of tautomers or conformers in varying relative amounts, which was used, for example, to explain the difference in intensities of similar double oxygen 1s peaks in cytosine and guanine.[45,46] The

TABLE II. Calculated binding energies (BEs) for HTI (a), HTI-OMe (b), and HTI-SMe (c) at the oxygen 1s edge for each oxygen atom. The BE values have been shifted by +0.35 eV in agreement with the plots in Fig. 3. In HTI-OMe, O1 and O2 refer to the carbonyl and methoxy oxygen atoms, respectively. For orbital labeling, consult Figs. S6 and S7 of the supplementary material.

Oxygen 1s edge			
(a) HTI			
Transition	BE (eV)	Dyson norm	Leading CSFs (weight)
$O1_1$	536.69	0.36	O(1s) ionization (0.72)
$O1_2$	538.69	0.05	O(1s) ionization + 9 → 11 shake-up (0.53)
$O1_3$	538.98	0.03	O(1s) ionization + 10 → 11 shake-up (0.45)
$O1_4$	540.16	0.05	O(1s) ionization + 6 → 11 shake-up(0.32)
(b) HTI-OMe			
Transition	BE (eV)	Dyson norm	Leading configuration state functions (CSFs) (weight)
$O1_1$	536.46	0.35	O1(1s) ionization (0.72)
$O1_2$	538.66	0.10	O1(1s) ionization + 10 → 11 shake-up (0.34) O1(1s) ionization + 9 → 11 shake-up (0.15)
$O2_1$	539.27	0.68	O2(1s) ionization (0.68)
(c) HTI-SMe			
Transition	BE (eV)	Dyson norm	Leading CSFs (weight)
$O1_1$	536.14	0.31	O1(1s) ionization (0.71)
$O1_2$	538.10	0.04	O1(1s) ionization + 10 → 11 shake-up (0.34) O1(1s) ionization + 9 → 11 shake-up (0.09)
$O1_3$	538.30	0.05	O1(1s) ionization + 9 → 11 shake-up (0.36) O1(1s) ionization + 10 → 11 shake-up (0.09)

comparison of HTI and HTI-SMe XPS spectra excludes this hypothesis. The new peak must originate solely from the additional methoxy oxygen ($O2_1$). However, it is well-known that intensity differences can also occur due to several non-stoichiometric effects, in particular electronic relaxation effects and intramolecular scattering effects.[47,48] EXAFS-like oscillations of the absorption cross section may occur, and these are the strongest at energies not far above the threshold, as in the present case.[47] The comparison with theory allows us to rule out EXAFS-like oscillations as the main contribution to this difference. Calculations predict a 2.8 eV chemical shift between the two oxygens and accurately reproduce the relative intensities, with O2 exhibiting a Dyson norm nearly twice as large (0.68) as the Dyson norm of O1 (0.36). Since scattering effects are not included in the calculations, the difference cannot be attributed to EXAFS-like oscillations. Instead, the intensities and chemical shifts of the two main peaks are correlated and reflect the different levels of electronic relaxation in the core-ionized states of the two oxygen atoms. As noted by Travnikova *et al.*,[48] the decrease in the main line due to electronic relaxation is normally on the order of about ≤10% but can be greater for aromatic donor–acceptor molecules. The observed decrease in $O1_1$ is exceptionally strong and indicates a strong final state relaxation effect. Indeed, conjugation of the carbonyl oxygen in the π-system through a single π-electron leads to a more pronounced electronic density reorganization in the π-system upon ionization compared to the methoxy oxygen, which participates through a lone pair. On the one hand, this allows for a more efficient shielding of the electronic charge density and manifests in a substantial redshift of the BE of the carbonyl oxygen compared to the methoxy oxygen. In fact, the difference in unrelaxed BE of the two oxygen atoms is only 0.4 eV (see the supplementary material, Table II), whereas upon considering relaxation, it increases to nearly 3 eV, thus underscoring the importance of this effect. On the other hand, the stronger relaxation leads to a decreased resemblance of the neutral and ionic wave functions, which is manifested in a lower Dyson norm of the main peak.

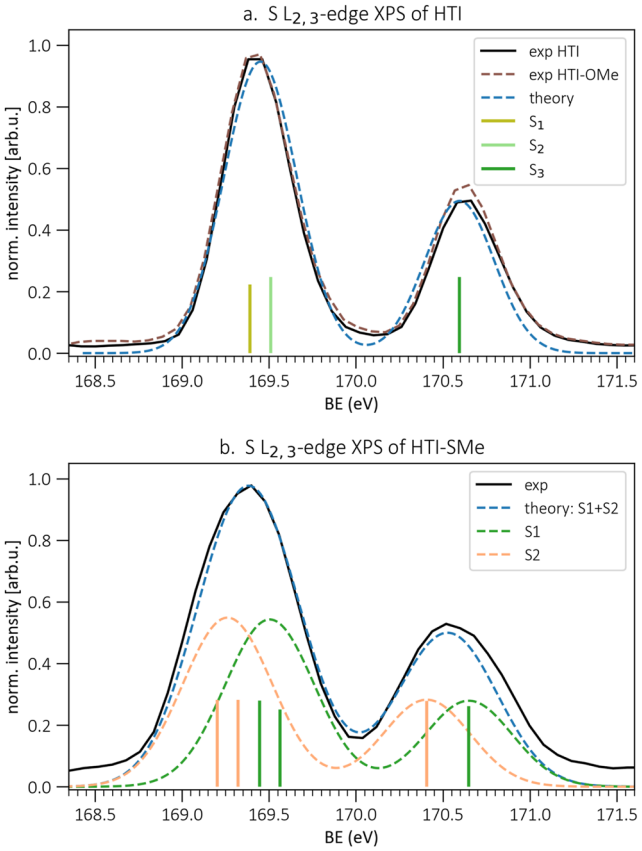

FIG. 4. Experimental (black line) and calculated (dashed line) sulfur 2p XPS spectra of HTI (a) and HTI-SMe (b). Panel (a) also shows the calculated spectrum for HTI-OMe. The calculated spectra have been shifted by +0.25 eV in order to match the experiment. The contribution of spin–orbit coupling is evident in the HTI spectrum and in the HTI-SMe spectrum, where the breaking of energy degeneracy by the molecular field is shown with vertical sticks. In HTI-SMe, the dashed blue curve is obtained by summing the contributions coming from two different sulfur atoms (S1 and S2). For the numbering of the S atoms, see Fig. 1.

3. Sulfur 2p ionization

The experimental and theoretical XPS spectra for the three samples, at the sulfur $L_{2,3}$-edge, are shown in Fig. 4. Computations were performed only for HTI and HTI-SMe, as the experimental spectrum of HTI-OMe is identical to that of HTI (black solid line vs brown dashed line). Tables III(a) and III(b) present the binding

TABLE III. Calculated binding energies (BEs) for HTI (a) and HTI-SMe (b) at the sulfur 2p edge. The BE values have been shifted by +0.25 eV in agreement with the plots in Fig. 4. In HTI-SMe, S1 and S2 refer to the benzothiophene and thiomethyl sulfur atoms, respectively. When spin–orbit coupling (SOC) is not considered, each sulfur exhibits a triad of degenerate core-ionizations with energies reported in the column BE without SOC. SOC causes each triad to split asymmetrically into two peaks, whose BEs are shown in the column BE. All ionization processes have Dyson norms of 1.47. For details on the wave functions with and without SOC, consult https://doi.org/10.6092/unibo/amsacta/8038.

Sulfur 2p edge			
(a) HTI			
Transition	BE (eV)	Leading CSFs	BE without SOC
S_1	169.60	S(2p) ionization	
S_2	169.75	S(2p) ionization	169.85–170.05
S_3	170.80	S(2p) ionization	
(b) HTI-SMe			
Transition	BE (eV)	Leading CSFs	BE without SOC (eV)
$S1_1$	169.45	S1(2p) ionization	
$S1_2$	169.55	S1(2p) ionization	169.75–169.95
$S1_3$	170.65	S1(2p) ionization	
$S2_1$	169.20	S2(2p) ionization	
$S2_2$	169.30	S2(2p) ionization	169.55–169.75
$S2_3$	170.40	S2(2p) ionization	

energies (BEs) for HTI and HTI-SMe, respectively. The tables include values for both spin-diabatic states (eigenstates without SOC) and spin-adiabatic states (eigenstates with SOC).

In all spectra, we observe a double peak feature peaking at 169.5 and 170.5 eV due to the SOC effect at the $L_{2,3}$ edge, which causes the 2p levels to split into a lower lying fourfold degenerate $2p_{3/2}$ state and a higher lying twofold degenerate $2p_{1/2}$ state. The magnitude of the splitting is ~1.2 eV, in agreement with previous work on thionated organic systems.[42] Moreover, the anisotropy of the system gives rise to a molecular field splitting of the $2p_{3/2}$ level into two components, S_1 and S_2.

The S 2p BE of HTI-SMe exhibits a chemical shift of around 0.15 eV to lower energy, accompanied by a pronounced broadening of the line shape. The broadening is reproduced by our simulations and is due to the slightly different chemical shifts of the benzothiophene (S1) and thiomethyl (S2) sulfur atoms (respectively, green and orange components of the spectrum in Fig. 4). The small BE difference (0.2 eV) and comparable Dyson norms (0.7) indicate that both sulfur atoms are subject to comparable initial and final state effects (unlike what is observed for the two oxygen atoms in HTI-OMe). This can be rationalized by considering that both sulfur atoms are conjugated in the π-system through a lone pair and are bonded via two single bonds to two carbon atoms. As observed for the methoxy oxygen, this leads to a weak electronic relaxation in

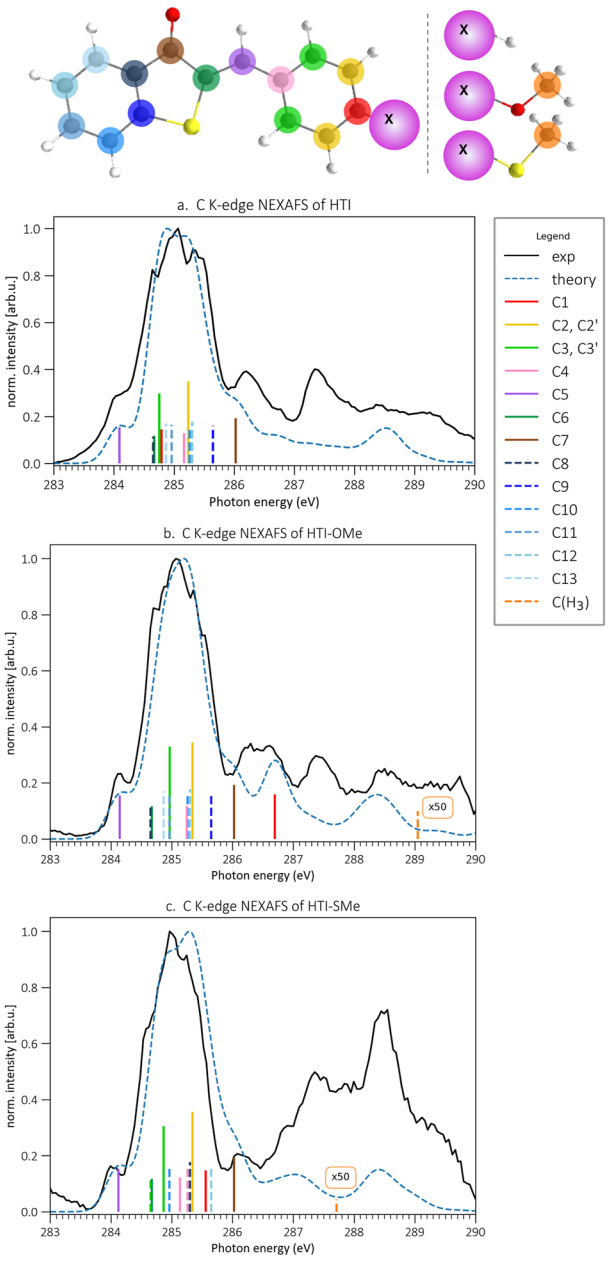

FIG. 5. C 1s NEXAFS spectra of HTI (a), HTI-OMe (b), and HTI-SMe (c). The sticks represent single C 1s → LUMO transitions. The high energy features arise from a convolution of a manifold of low intensity transitions toward higher virtual orbitals (Fig. S1 of the supplementary material). For the numbering of the C atoms, see Fig. 1, and for the color coding in the legend, see the figure above.

TABLE IV. Calculated core excited states of HTI (a), HTI-OMe (b), and HTI-SMe (c) at the carbon 1s edge. Table (a) lists the transition energies for each carbon in HTI, while Tables (b) and (c) report the transition energies only for those carbon atoms of HTI-OMe and HTI-SMe that show significant chemical shifts with respect to HTI (relative shift reported in boldface in parentheses) together with the transition energy of the carbon of the methoxy and thiomethyl groups. For the numbering of the C atoms, see Fig. 1. For orbital labeling, consult Fig. 6 and Figs. S10 and S11 of the supplementary material.

Carbon 1s edge

(a) HTI

Transition	Energy (eV)	Osc. strength	Leading CSFs
C_1	284.80	0.036	C1 → 11
$C_{2,2'}$	285.25	0.040(x2)	C2/C2' → 11
$C_{3,3'}$	284.80	0.037 (x2)	C3/C3' → 11
C_4	285.15	0.032	C4 → 11
C_5	284.10	0.038	C5 → 11
C_6	284.65	0.029	C6 → 11
C_7	286.00	0.048	C7 → 11
C_8	284.65	0.028	C8 → 11
C_9	285.65	0.040	C9 → 11
C_{10}	285.25	0.037	C10 → 11
C_{11}	284.95	0.041	C11 → 11
C_{12}	285.30	0.039	C12 → 11
C_{13}	284.85	0.042	C13 → 11

(b) HTI-OMe

Transition	Energy (eV)	Osc. strength	Leading CSFs
C_1	286.70 (**+1.90**)	0.040	C1 → 11
$C(H_3)$	289.047		No intense signal

(c) HTI-SMe

Transition	Energy (eV)	Osc. strength	Leading CSFs
C_1	285.55 (**+0.75**)	0.037	C1 → 11
$C(H_3)$	287.71		No intense signal

the final ionized state, which is reflected in the high pole strength. To reinforce this statement, we computed the sulfur BE for an HTI derivative in which the carbonyl oxygen is replaced by a sulfur atom (supplementary material, Chap. VIII). Similar to the carbonyl oxygen in HTI, the thiocarbonyl sulfur shows a strongly redshifted BE (2.2 eV with respect to the thioindigo sulfur), accompanied by a pronounced decrease of the Dyson intensity to 0.4 (compared to 0.75 of the thioindigo sulfur).

B. NEXAFS spectra

1. Carbon K edge

Figure 5 shows the NEXAFS spectra of the three samples taken at the carbon K-edge. Colored sticks indicate the energies and relative intensities of the transitions from the core to the lowest unoccupied π^* orbital (LUMO) for each carbon atom. Transitions to higher lying π^* orbitals are not indicated by sticks due to their overall low intensities (see the supplementary material at https://doi.org/10.6092/unibo/amsacta/8038), but they are taken into account in the total spectra shown with dashed blue lines. Table IV(a) lists the C 1s → LUMO transition energies for each carbon, while Tables IV(b) and IV(c) report the transition energies for C1, the only center showing a notable shift upon functionalization, together with the carbon in the substituent group.

At low energy, we observe an intense signal common to all three spectra, very similar for all three samples, and which is in good agreement with the theoretical prediction. Moving to higher energies (>286.5 eV), the agreement between experiment and simulation gets worse. In particular, the total intensity of the computed signal is insufficient to describe the intense and broad absorption feature observed experimentally. Simulations by Toffoli *et al.* on benzothiophene assigned the spectral bands above 286.5 eV to transitions to virtual MOs of σ^*, Rydberg, and mixed character. The methodology used in our work is by construction blind to these signatures, as the active space comprises only π^*-type virtual orbitals. In Chap. X of the supplementary material, we discuss an effort to recover these missing features in the case of HTI by performing an additional set of calculations, replacing the π^* MOs with 30 virtual MOs.

In the following discussion, we focus on the main peak between 284 and 286 eV, which is due to the C 1s → LUMO transition from all carbon atoms (Fig. 6). We draw attention to the shoulders in the spectra of all three species at lower (284 eV) and higher (286 eV) energies, which are associated with the C5 1s → LUMO and C7 1s → LUMO, respectively. The BE of C5 does not show any observable difference from the BE of the remaining carbon atoms (see XPS spectra in Fig. 2), while it is evidently redshifted with respect to the main peak in the NEXAFS spectrum. C7, the carbon atom of the carbonyl group, exhibits a much less pronounced blueshift in the NEXAFS spectra with respect to the remaining carbon atoms compared to the XPS case. As will be discussed in more detail in Sec. IV, these shifts can be rationalized by the relative weights of the individual carbon atoms in the wave function of the LUMO (Fig. 6) and,

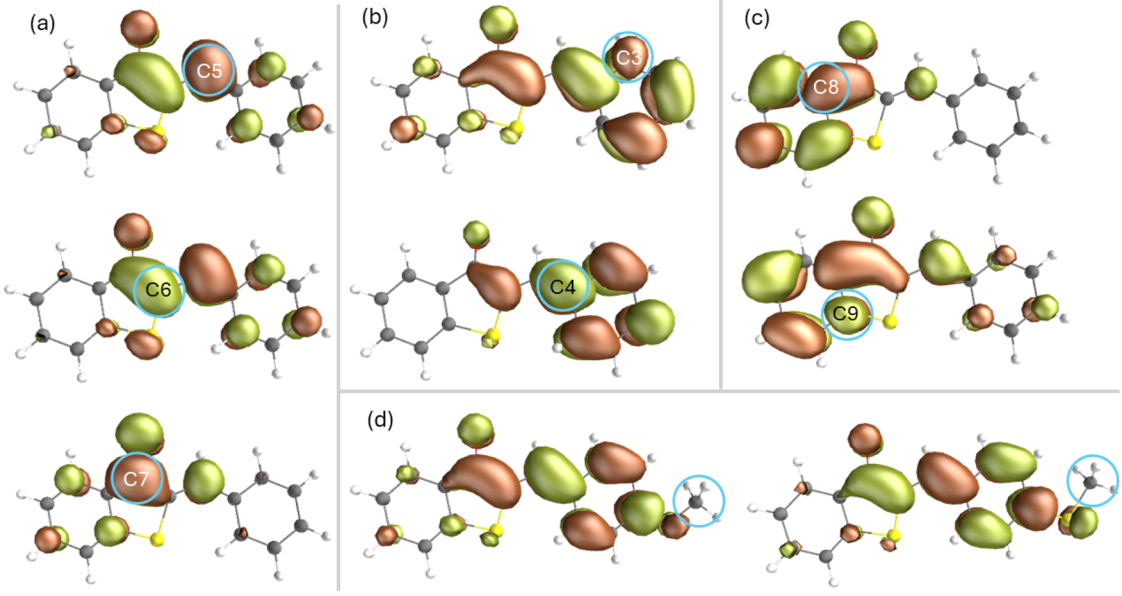

FIG. 6. Selected LUMO relaxed to the 1*s* → LUMO core-excited electronic state of individual carbon atoms (highlighted by a circle) of HTI (a)–(c), HTI-OMe [(d), left], and HTI-SMe [(d), right]. For labels, see Fig. 1.

thus, by the stronger Coulomb attraction between the core-hole and the core-excited electron.

As already mentioned, upon functionalization, C1 is the only center that undergoes a significant chemical shift, +1.90 eV for −OMe and +0.75 eV for −SMe, while all other carbon atoms show negligible shifts (within ±0.1 eV). The large shift in HTI-OMe could explain the broader shoulder spanning from 286 to 287 eV. The finding that other carbon atoms from the phenyl group are practically unaffected, unlike what was observed in the XPS spectra, indicates that mesomeric effects do not play a significant role in core excitations. This observation can be understood if one considers that the core-excited electron occupies a virtual π^* orbital and is utilized to shield the core hole; thus, it is no longer necessary to withdraw density from the functional group over the π-system.

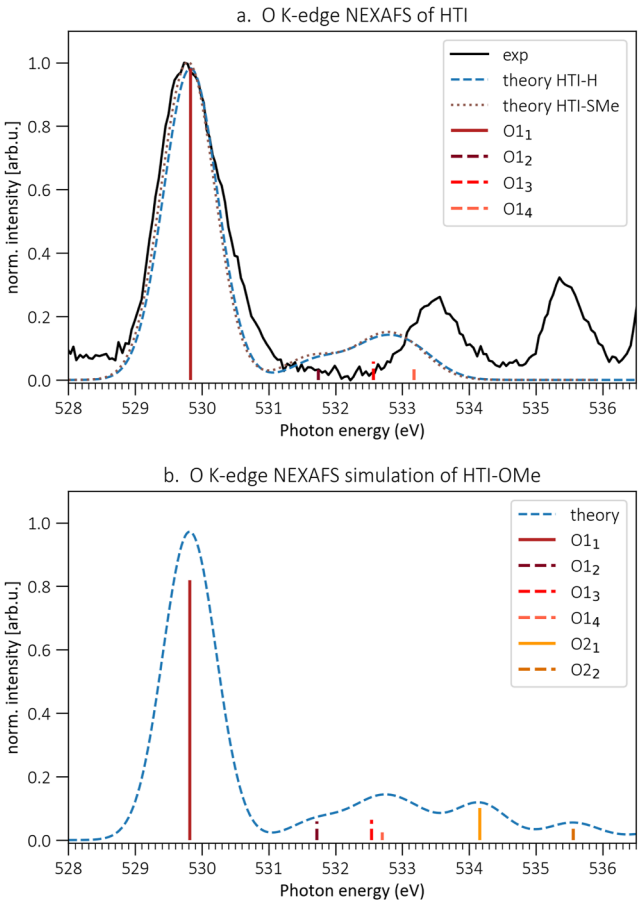

FIG. 7. Calculated O 1s NEXAFS spectra of (a) HTI (dashed line) and HTI-SMe (dotted line) and (b) HTI-OMe (dashed line) together with experimental data (solid line) measured only for HTI (a) (solid black line). The calculated spectra have been shifted by −0.55 eV in order to match the experiment. In HTI-OMe, O1 and O2 refer to the carbonyl and methoxy oxygen atoms, respectively. The dashed vertical lines represent the energies of the shake-up features. The peaks at energies above 531 eV in the experimental HTI spectrum (a) arise from residual water in the chamber.

TABLE V. Calculated core excited states of HTI (a), HTI-OMe (b), and HTI-SMe (c) at the oxygen 1s edge for each oxygen atom. The energy values have been shifted by −0.55 eV in agreement with the plots in Fig. 7. In HTI-OMe, O1 and O2 refer to the carbonyl and methoxy oxygen atoms, respectively. For orbital labeling, consult Figs. S12 and S13 of the supplementary material.

Oxygen 1s edge			
(a) HTI			
Transition	Energy (eV)	Osc. strength	Leading CSFs (weight)
O1$_1$	529.82	0.030	O(1s) → 11 (0.75)
O1$_2$	531.75	0.002	O(1s) → 11 + 10 → 11 shake-up (0.16)
			O(1s)+ 14 (0.14)
			O(1s) → 11 + 8 → 11 shake-up (0.11)
O1$_3$	532.56	0.002	O(1s) → 11 + 7 → 11 shake-up (0.13)
			O(1s) → 12 (0.10)
			O(1s) → 11 + 10 → 11 shake-up (0.10)
O1$_4$	533.17	0.002	O(1s) → 11 + 6 → 11 shake-up (0.27)
			O(1s) → 16 (0.11)
(b) HTI-OMe			
Transition	Energy (eV)	Osc. strength	Leading CSFs (weight)
O1$_1$	529.81	0.030	O1(1s) → 11 (0.76)
O1$_2$	531.71	0.002	O1(1s) → 11 + 10 → 11 shake-up (0.16)
			O1(1s) → 15 (0.14)
			O1(1s) → 14 (0.06)
O1$_3$	532.54	0.002	O1(1s) → 11 + 7 → 11 shake-up (0.13)
			O1(1s) → 11 + 9 → 11 shake-up (0.10)
			O1(1s) → 16 (0.10)
O1$_4$	533.15	0.002	O1(1s) → 11 + 6 → 11 shake-up (0.26)
			O1(1s) → 13 (0.11)
O2$_1$	534.16	0.004	O2(1s) → 11(0.76)
O2$_2$	535.56	0.002	O2(1s) → 15 (0.26)
			O2(1s) → 14 (0.15)
			O2(1s) → 16 (0.13)
			O2(1s) → 16 (0.10)
(c) HTI-SMe			
Transition	Energy (eV)	Osc. strength	Leading CSFs (weight)
O1$_1$	529.79	0.030	O(1s) → 11 (0.75)
O1$_2$	531.75	0.002	O(1s) → 11 + 10 → 11 shake-up (0.22)
			O(1s) → 14 (0.12)
			O(1s) → 18 (0.11)
O1$_3$	532.57	0.002	O(1s) → 11 + 7 → 11 shake-up (0.15)
			O(1s) → 12 (0.12)
O$_4$	533.08	0.002	O(1s) → 11 + 4 → 11 shake-up (0.28)
			O(1s) → 13 (0.12)

Finally, the carbon of the methyl group in HTI-OMe and HTI-SMe [indicated by C(H$_3$) in Table IV] does not exhibit any intense transition, the reason being that this carbon is not part of the aromatic system and does not contribute an orbital of π character to

any of the low lying π^* orbitals [see Fig. 6(d)]. As the signal intensity in NEXAFS spectroscopy is determined by the spatial overlap between the core and the virtual orbitals, the absence of a methyl carbon contribution to the virtual π^* orbital renders all its transitions to the latter optically dark.

2. Oxygen 1s edge

Figure 7 shows the oxygen K-edge NEXAFS spectra. The experimental spectra were taken only for HTI, while simulations were instead generated for all the samples. Tables V(a)–V(c) report the transition energies.

All three spectra show a common feature at 529.8 eV, exhibiting a weak asymmetric broadening due to vibronic effects, and the peak is attributed to an O 1s → LUMO transition of the carbonyl oxygen (cyan, $O1_1$). The simulations indicate that the band does not undergo a shift upon functionalization with either OMe or SMe. The experimental HTI spectrum shows two peaks at higher energies (>531 eV) that arise from residual water in the chamber and that cover any other theoretically predicted shake-up features (dashed vertical red lines in Fig. 7). Compared to the electron analyzer used for XPS, the channel electron multiplier used for NEXAFS detects a wider volume, including regions where the density of the sample is smaller, and so is more sensitive to the residual gas.

The simulated spectrum of HTI-OMe reveals transitions at energies above 534 eV coming from the methoxy oxygen (orange, O2). As in the XPS counterpart, these transitions require more energy. In particular, the O 1s → LUMO transition peaks at 534.2 eV, i.e., at 4.5 eV higher energy. However, none of the transitions involving the methoxy oxygen are intense due to the low overlap between the core-orbital and the virtual π^* orbitals. Figure 8 demonstrates this for the example of the LUMOs relaxed to the 1s → LUMO core-excited states of the two oxygen atoms. One can appreciate the vanishingly small MO coefficient for O2.

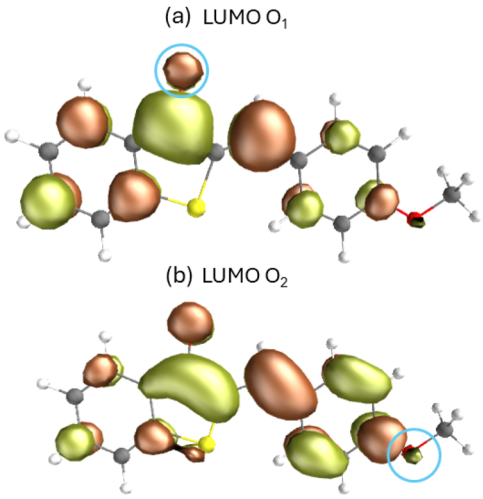

FIG. 8. LUMO optimized in the core-excitations of the carbonyl (a) and methoxy (b) oxygen atoms of HTI-OMe.

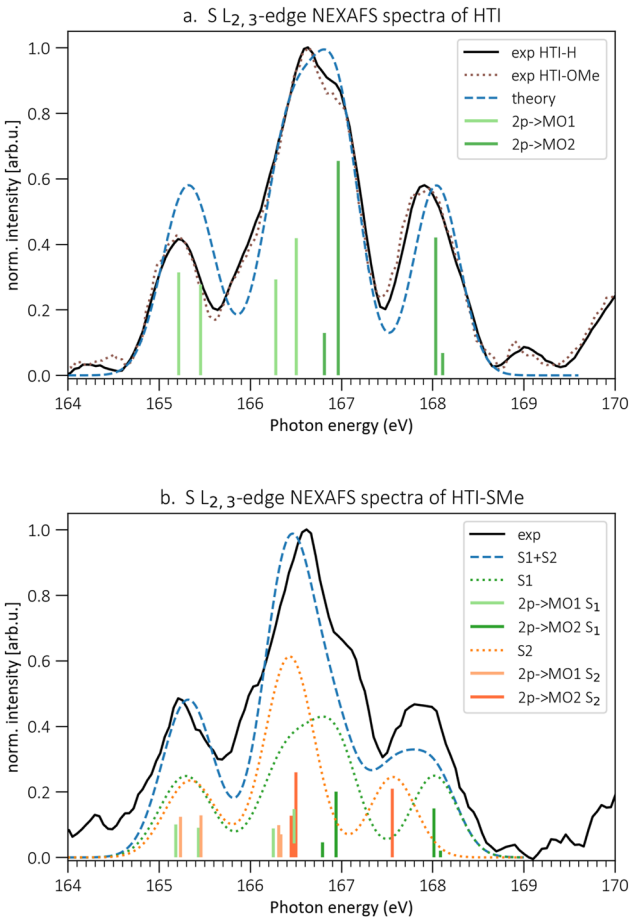

FIG. 9. S $L_{2,3}$ NEXAFS spectra of HTI (a) and HTI-SMe (b). The calculated spectra (dashed line) have been shifted by −0.40 eV in order to match the experiment (solid black line). S1 and S2 in HTI-SMe refer to the benzothiophene and thiomethyl sulfur atoms, respectively. The sticks indicate transitions to orbitals localized around each sulfur atom, denoted as LUMO and LUMO+1 (Fig. 10), each of which is spin–orbit split.

3. Sulfur 2p edge

Figure 9 shows the NEXAFS spectra at the sulfur $L_{2,3}$-edge. Computations were performed only for HTI and HTI-SMe, as the spectrum of HTI-OMe is identical to that of HTI (black solid line vs brown dashed line). Table VI reports the transition energies for the spin-diabatic and spin-adiabatic states.

All spectra present a common feature with three peaks between 165 and 169 eV that show little change between the samples.

TABLE VI. Calculated core excited states of HTI (a) and HTI-SMe (b) at the sulfur 2p edge. The energy values must be shifted by −0.40 eV in agreement with the plots in Fig. 9. S1 and S2 in HTI-SMe refer to the benzothiophene and thiomethyl sulfur atoms, respectively. When spin–orbit coupling (SOC) is not considered, each sulfur exhibits triads of degenerate core-transitions to orbitals localized around each sulfur atom, denoted as LUMO and LUMO+1 (Fig. 10), with energies reported in the column Energy without SOC. SOC causes each triad to split asymmetrically into two peaks whose energies are shown in the column Energy. The reported oscillator strengths are cumulative over the signals in the reported window. For details on the wave functions with and without SOC, consult https://doi.org/10.6092/unibo/amsacta/8038.

Sulfur 2p edge				
(a) HTI				
Range	Energy (eV)	Osc. strength	Leading CSFs	Energy without SOC (eV)
S_1	165.2–165.4	0.015	S(2p) → LUMO	165.7–166.1
S_2	166.3–166.5	0.018	S(2p) → LUMO	
S_3	166.8–166.9	0.018	S(2p) → LUMO+1	167.4–167.6
S_4	168.0–168.1	0.013	S(2p) → LUMO+1	
(b) HTI-SMe				
Range	Energy (eV)	Osc. strength	Leading CSFs	Energy without SOC (eV)
$S1_1$	165.2–165.4	0.015	S1(2p) → S1(LUMO)	165.7–166.1
$S1_2$	166.3–166.5	0.018	S1(2p) → S1(LUMO)	
$S1_3$	166.8–166.9	0.018	S1(2p) → S1(LUMO+1)	167.4–167.6
$S1_4$	168.0–168.1	0.013	S1(2p) → S1(LUMO+1)	
$S2_1$	165.2–166.4	0.014	S2(2p) → S2(LUMO)	165.6–166.1
$S2_2$	166.3	0.005	S2(2p) → S2(LUMO)	
$S2_3$	166.3–166.5	0.028	S1(2p) → S2(LUMO+1)	166.9–167.2
$S2_4$	167.6–167.7	0.012	S1(2p) → S2(LUMO+1)	

This peak profile has already been documented for other sulfur-containing species such as (oligo)-thiophenes, benzothiophene, and dibenzothiophene.[42,49] The central peak shows a fine structure with a shoulder at lower energies in HTI and HTI-OMe and a shoulder at higher energies in HTI-SMe.

Calculations show that the HTI signal arises from the overlap of core-transitions to a pair of MOs, labeled MO1 and MO2, localized on the benzothiophene sulfur (S1) [see Fig. 10(a)], modulated by the SOC. In particular, in the absence of SOC, the two sets of core-transitions peak at about 165.9 eV (S 2p → MO1, light green) and 167.5 eV (S 2p → MO2, dark green). The SOC of about 1.2 eV magnitude splits the signals, making the high energy $2p_{1/2}$ component of the 165.9 eV peak overlap with the low energy $2p_{3/2}$ component of the 167.9 eV peak in the window between 166 and 167 eV, explaining the increased intensity and the shoulder shifted to the red of the central peak.

The two sulfur atoms in HTI-SMe show similar signal patterns, as the virtual orbitals involved in the bright transitions have very similar shapes (see Fig. 10). In fact, the 2p → MO1 transitions of the benzothiophene sulfur (S1) and the thiomethyl sulfur (S2) atoms coincide (light green and red sticks). Instead, the 2p → MO2 transitions of S2 (dark green and red peaks) show a 0.4 eV shift toward lower photon energy relative to the 2p → MO2 transitions of S1. This could explain the shoulder in the central peak (at 167 eV) and the slightly broader line shape of the peak at 168 eV in the spectrum of HTI-SMe compared to HTI.

The virtual orbitals have contributions from 3d to 4s atomic basis functions on the sulfur, in agreement with the selection rules in atoms, namely, that $\Delta l = \pm 1$ for a transition to be allowed. Overall, the lack of significant differences between the spectra of the three molecules is due to the fact that the virtual orbitals involved in the sulfur $L_{2,3}$ edge are localized on the sulfur atoms; thus, they are not involved in the π-system and are not affected by functionalization. This observation will be further addressed in Sec. IV.

IV. DISCUSSION

In the following, we scrutinize the observed variation of signal intensities and chemical shifts in the series of HTI compounds.

A. Chemical shift and intensity in XPS

K-edge XPS spectra usually exhibit one intense peak per atom associated with the BE of its 1s core orbital as well as multiple less intense features—known as shake-ups or two-hole, one-particle final states—at higher energy, with valence excitations accompanying the core-ionization. These shake-up features can be best observed in the O 1s spectra above 538 eV (Fig. 3).

The effect of the chemical environment is most clearly appreciable in HTI-OMe, which includes two markedly different oxygen species, a carbonyl and a methoxy group. As a consequence, HTI-OMe shows two distinct intense peaks in the spectrum [Fig. 3(b)],

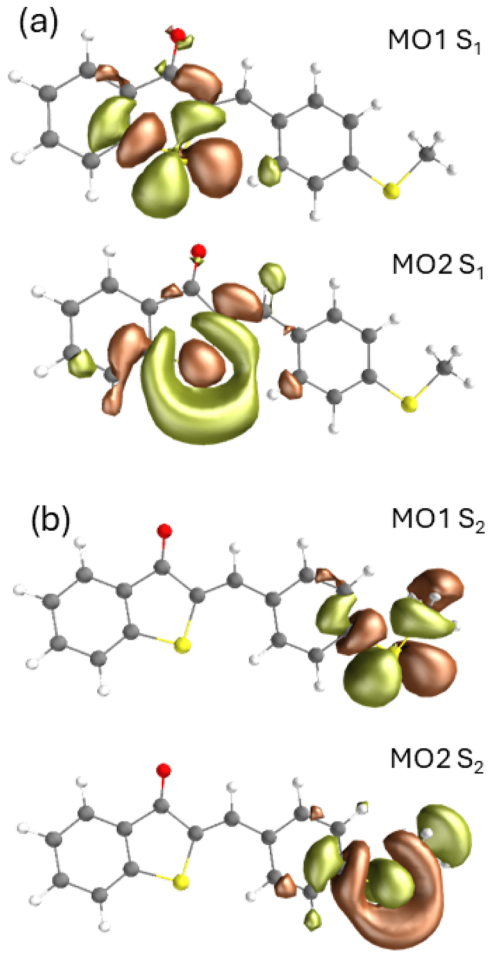

FIG. 10. LUMO and LUMO+1 optimized in the core-excitations of the benzothiophene (a) and thiomethyl (b) sulfur atoms of HTI-SMe.

one at 536.5 eV and another one at 539.3 eV, with the high energy peak exhibiting twice the intensity. The simulations and the direct experimental comparison with HTI allowed us to attribute these peaks to the carbonyl and methoxy oxygen atoms, respectively, thereby revealing that the higher intensity of the latter is *not* due to overlap with shake-up features. In fact, only one shake-up at 538.7 eV contributes with notable intensity in the window of the methoxy peak. The difference in intensity is rather related to the value of the Dyson norm (0.68 vs 0.35), which reflects the different relaxation of the electron density after ionization.[50] The closer to unity the value of the Dyson norm, the greater the similarity of the neutral and cation wave functions. Our simulations show that the Dyson intensity is related to the way the heteroatom is conjugated in the π-system. The carbonyl oxygen contributes a single electron whose 2p atomic orbital participates in several π and π^* MOs (Fig. S4 of the supplementary material). Due to its increased electronegativity, upon ionization, the carbonyl oxygen attracts electron density over the aromatic system, which leads to the effective decoupling of the 2p orbital from the π-system and its localization around the heteroatom (MO2 in Fig. S6). The electron relaxation in the π-system alters considerably the wave function of the cation, causing a strong decrease of the Dyson norm to values below 0.4. The decrease in the pole strength is accompanied by a strong (i.e., up to several eV) redshift of the BE. Instead, the methoxy oxygen donates a lone pair that remains mostly localized on the heteroatom in both the neutral and the core-ionized forms. Accordingly, the Dyson norm shows values closer to unity.

The reasoning also extends to sulfur. Unlike its methoxy counterpart, both sulfur atoms in HTI-SMe donate lone pairs that remain primarily localized on the heteroatom. As a result, the XPS $L_{2,3}$ edge spectrum of HTI-SMe exhibits overlapping signals from the two sulfur atoms. Instead, sulfur atoms participating through a single electron in the π-system are expected to show a redshift and lower pole strength, much like the HTI carbonyl oxygen, as demonstrated by XPS simulations of a thiocarbonyl HTI derivative.

Turning our attention to carbon, we note that the Dyson norms of the methoxy and thiomethyl carbon atoms—the only carbon not part of the π-system—have a higher value (0.73) compared to the Dyson norms of the conjugated carbon atoms (0.62–0.66), the reason being that upon ionization each conjugated carbon is able to attract electron density over the aromatic system, which leads to a stronger reorganization of the wave function. The small decrease in the Dyson norm compared to oxygen is a consequence of the different electronegativity of carbon and oxygen. Oxygen, being more electronegative, causes a stronger rearrangement of the wave function upon ionization, which reduces more markedly the overlap with the neutral state.

The carbon edge spectral region offers a platform for examining the effect of functional groups on the chemical shift. For HTI, our simulations demonstrate that almost all carbons have BEs in a region of ±0.3 eV around the main peak, which is found experimentally at 290.3 eV. Outliers are the signals from C9 and C7 blueshifted by 0.7 and 2.3 eV with respect to the main peak, respectively. Regarding C7, this blueshift can be traced back to the immediate vicinity of oxygen. In particular, a carbon attached to a heteroatom with higher electronegativity (N, O, F) is expected to exhibit a blueshift of up to several electronvolts due to the strong negative inductive effect and, as in the case of carbonyl or imine groups, negative mesomeric effects in the ground state (initial state effect). As for the blueshift of C9, such a trend was already observed in polycyclic aromatic hydrocarbons for carbon atoms not bonded to any hydrogen.[51]

C1 and the $C(H_3)$ carbon atoms in the functionalized HTIs require an additional discussion. Due to the different electronegativity of S and O, the blueshift of these two contributions with respect to the other carbons is lower for HTI-SMe than for HTI-OMe (initial-state effect). Furthermore, since the $C(H_3)$ carbon atom does not participate in the aromatic ring, its additional blueshift of ≈1 eV can be attributed to its lower ability to attract electrons from the aromatic ring upon ionization compared to all the other carbons (final-state effect).

The theoretical calculations allow us to draw further conclusions about the positive mesomeric effect (+M) that the methoxy and thiomethyl groups additionally exercise in conjugated and aromatic systems. This effect gives the phenyl carbon atoms access to excess electron density to better shield the positive charge created upon ionization. Consequently, the BE of the phenyl carbon atoms redshifts upon functionalization in both HTI-OMe and HTI-SMe.

Notably, the mesomeric effect is not linear as a function of the distance from the functionalization site. This can be appreciated by the more pronounced (0.2–0.3 eV) BE redshifts for carbon atoms C2, C2′ (ortho), and C4 (para) compared to the almost absent shift for carbon atoms C3 and C3′ (meta). This can be rationalized in terms of the mesomeric Lewis structures that can be drawn to illustrate the propagation of the +M effect in the aromatic molecule (Fig. S17 of the supplementary material).

B. Chemical shift and intensity in NEXAFS

In contrast to XPS, NEXAFS spectra may exhibit multiple intense transitions of each atom, as there are a number of virtual MOs to host the core-excited electron. Shake-up features are also observed in NEXAFS spectra, yet they often mix with other transitions so that the low intensity peaks can rarely be assigned exclusively to either of the two processes (see NEXAFS spectra at the oxygen K-edge as an example, Fig. 7). Overall, the NEXAFS spectrum is more congested, and chemical shifts and signal intensity depend on both core and virtual orbitals, which complicates the analysis. Still, several general conclusions can be drawn by comparing HTI and its derivatives.

Regarding K-edge spectra, atoms conjugated in the π-aromatic systems through a single electron participate in the virtual π orbitals, leading to bright transitions. Examples thereof are the 1s → LUMO transitions of the carbonyl oxygen [peak at 529.8 eV in Fig. 7(a) and the LUMO shown in Fig. 8(a)] and of all carbon atoms [Fig. 5(a) and the LUMO shown in Figs. 6(a)–6(c)] in HTI. Conversely, atoms that conjugate in the π-aromatic systems through a pair of electrons participate almost exclusively in the occupied π orbitals and hence do not exhibit bright transitions in the NEXAFS spectrum. This is the case with the methoxy oxygen in HTI-OMe, whose 1s → LUMO transition is characterized by an oscillator strength an order of magnitude smaller compared to the carbonyl oxygen [Fig. 7(b); the LUMO is shown in Fig. 8]. Finally, atoms not participating in the π-system do not show intense low lying pre-edge signals. This is illustrated by the absence of a signal from the methyl carbon at the K-edge of HTI-OMe and HTI-SMe [the LUMO is shown in Fig. 6(d)].

Regarding $L_{2,3}$-edge spectra, we emphasize that those are dominated by transitions to final states localized around the heteroatom with contributions from 3d to 4s atomic orbitals, in agreement with the atomic dipole selection rules. 2p → π^* transitions, instead, are one to two orders of magnitude weaker. As discussed in Sec. III, the sulfur $L_{2,3}$ edge in HTI is dominated by two transitions to virtual orbitals with large 3d and 4s components (Fig. 10), in good agreement with the experiment. Notably, due to their spatial distribution, highly localized around the sulfur, these virtual orbitals remain mostly unaffected by the functionalization of the π-system. In fact, the spectra of HTI, HTI-OMe, and HTI-SMe show pronounced similarity and no spectral shifts with respect to each other. The lack of sensitivity of the final states to changes in the π-system leads to the conclusion that NEXAFS $L_{2,3}$ spectra have the same informational content regarding chemical shifts as XPS spectra.

As for the chemical shift of the contributions from individual carbon atoms, we found it to be dependent on the spatial distribution of the core-excited electron in the final state. Taking the K-edge of the carbon atoms in HTI as an example, we noted in Sec. III that the C5 1s → LUMO transition (pink in Fig. 5) is shifted to a considerably lower energy (284.1 eV) compared to the other centers. If one looks at the XPS spectrum instead, the signal of C5 is buried in the signals of other carbon atoms. Thus, we conclude that the redshift in the NEXAFS spectrum is caused by the spatial distribution of the virtual orbital, thereby increasing the Coulomb attraction between the hole and the core-excited electron. In fact, examining the relaxed LUMOs of all carbon core-transitions [Figs. 6(a)–6(c)], we can sort them into three categories: LUMOs that localize in the center C5=C6–C7=O fragment [Fig. 6(a)], LUMOs that localize on the benzene ring of the hemistilbene [C1 through C4, Fig. 6(b)], and LUMOs that localize on the benzene ring of the benzothiophene [C8 through C13, Fig. 6(c)]. The first group exhibits the most localized LUMO with larger coefficients on atoms C5, C6, and C7. Consequently, in core-excited states involving C5, the excited electron has a higher probability of residing on the respective atom compared to core-excited states involving the carbon atoms of the benzene rings. This allows more efficient stabilization of the hole created in the 1s orbitals of C5 upon excitation, thus causing the redshift of the signal. The same reasoning applies to signals from C6 and C7. Carbon atoms of the benzene rings are subject to a LUMO delocalized over the entire six-member ring, which leads to a weaker hole-electron attraction.

Finally, the theory predicts that chemical shifts due to mesomeric effects are much weaker in NEXAFS spectra compared to their XPS counterparts. The BE of the phenyl carbon atoms does not show the redshift trend observed in XPS. It appears that the Coulomb attraction between the hole and core-excited electron residing in virtual valence orbitals supersedes the mesomeric effect of the electron donating groups. This observation might not extend to transitions to virtual orbitals of Rydberg type, which are expected to exhibit lower Coulomb attraction due to their diffuse nature. In such a case, electron-donating groups are expected to contribute to the relaxation upon core-excitation, thus leading to discernible shifts.

V. CONCLUSION

In this joint experimental and theoretical work, we studied the atomic sensitivity of HTI compounds with different types of functionalization using two complementary techniques: XPS and NEXAFS. This analysis allowed us to understand the role of atoms belonging to the second and third periods of the Periodic Table in core-level photoionization and photoexcitation of functionalized HTIs. These observations can guide us toward the selection of specific techniques for probing, locally, the charge transfer in conjugated and aromatic compounds.

XPS tells us that the chemical shift and intensity of core ionization are interlinked, as both depend on the way a heteroatom is conjugated in the π-system. Conjugation through a single electron (as is the case with carbonyl and thiocarbonyl groups) allows for a more pronounced wave function rearrangement in the ionized state, leading simultaneously to lower BE and lower pole strengths compared to conjugation through a lone pair. This is particularly evident in the HTI-OMe XPS case, where the two oxygens have different conjugations in the π-system, producing two well-separated peaks with different intensities. Compared to chemical shifts, which can result from both initial state and final state effects, variations in the

pole strengths arise solely from the electronic relaxation following photoionization. Consequently, the observed remarkable difference in intensities between the two oxygen peaks provides a direct experimental signature of the strong electronic relaxation process induced by core-level photoionization from highly conjugated heteroatoms.

NEXAFS provides insights into the excited states, as the oscillator strength and the chemical shift of core to virtual transitions depend on their spatial overlap. Transitions to virtual orbitals with significant MO coefficients at the core-excited atoms are more intense and appear redshifted due to the more efficient shielding of the charge density. At the sulfur $L_{2,3}$-edge, the HTI spectra in all the studied compounds are dominated by transitions to final states with contribution from 3d to 4s atomic orbitals of the heteroatom, which are less sensitive to chemical modifications in the π-system. Thus, at the $L_{2,3}$-edge, NEXAFS has the same informational content regarding chemical shifts as XPS. At the K-edge, only atoms conjugated in the π-system through a single electron contribute to the pre-edge, whereas heteroatoms contribute a lone pair to the π-system, and those that are not part of the π-system do not present intense peaks, as they do not contribute to virtual MOs.

Finally, functional groups exercise inductive and mesomeric effects that affect the chemical shift. This is particularly evident in carbon 1s XPS spectra, where atoms ortho and para to the functionalization site exhibit redshifted BEs. Instead, the inductive effect dominates at short distances. For example, the negative inductive effect of oxygen in HTI-OMe causes a strong blueshift of the BE of the ipso carbon.

Together, the insights gained from XPS and NEXAFS form a robust foundation for studying time-resolved charge transfer and photophysical processes in HTI photoswitches. Our results show that these two techniques are highly sensitive to the different chemical shifts of functionalized HTI dyes, even when only the ground state is probed. This sensitivity suggests that even more pronounced shifts can be expected in the excited state dynamics, involving highly polar intermediate states.[19] For this reason, we can anticipate that by combining XPS and NEXAFS, it will be possible to achieve a detailed understanding of the mechanism of ultrafast HTI photoisomerization and of the role of specific functional groups in tuning the excited state lifetimes.

SUPPLEMENTARY MATERIAL

See the supplementary material for details on the data analysis; IR spectra to assess the integrity of the samples; details on the simulation protocol; figures of the full active spaces used in the RASSCF/RASPT2 calculations of the carbon, oxygen, and sulfur valence; core-excited and core-ionized states; tables comparing core binding energies with relaxed and non-relaxed molecular orbitals; XPS spectra of the thiocarbonyl HTI derivative; mesomeric structure of HTI-OMe; and details on the simulation of the higher energy window (>286 eV) in the NEXAFS spectra at the K-edge of the carbon.

ACKNOWLEDGMENTS

M.D., D.F., G.C., M.G., and C.V. acknowledge the financial support under the National Recovery and Resilience Plan (NRRP), Mission 4, Component 2, Investment 1.1, Call for Tender No. 1409 published on September 14, 2022, by the Italian Ministry of University and Research (MUR), funded by the European Union—NextGenerationEU—Project No. P20224AWLB "HAPPY"—CUP B53D23025210001—Grant Assignment Decree No. 1386 adopted on September 01, 2023. M.D., D.F., and C.V. acknowledge the financial support under the National Recovery and Resilience Plan (NRRP), Mission 4, Component 2, Investment 1.1, Call for Tender No. 104 published on February 02, 2022, by the Italian Ministry of University and Research (MUR), funded by the European Union—NextGenerationEU—Project No. 20224KAC28 CHANGE—CUP B53D23013410006—Grant Assignment Decree No. 958 adopted on June 30, 2023, by the Italian Ministry of University and Research (MUR). M.D., M.C., and C.V. acknowledge the financial support under the National Recovery and Resilience Plan (NRRP), Mission 4, Component 2, Investment 1.1, Call for Tender No. 104, published on February 2, 2022, by the Italian Ministry of University and Research (MUR), funded by the European Union—NextGenerationEU—Project No. 2022K5W59T DEMIST—CUP B53D23013780006—Grant Assignment Decree No. 958 adopted on June 30, 2023, by the Italian Ministry of University and Research (MUR). L.O. and C.V. acknowledge the support of the "Center for Molecular Science" (CMWS). M.G. and A.N. acknowledge the financial support by the U.S. Department of Energy, Office of Science, Office of Basic Energy Sciences, Division of Chemical Sciences, Geosciences, and Biosciences under No. DESC0022225. P.B., L.A., L.C., and J.C. acknowledge the financial support under the PNRR-IR project EuPRAXIA Advanced Photon Sources—EuAPS (CUP I93C21000160006, IR0000030). We acknowledge the funding through the project EUROFEL-ROADMAP ESFRI of the Italian Ministry of University and Research.

AUTHOR DECLARATIONS

Conflict of Interest

The authors have no conflicts to disclose.

Author Contributions

L. Oberti: Data curation (lead); Formal analysis (equal); Investigation (equal); Methodology (equal); Validation (equal); Visualization (lead); Writing – original draft (equal); Writing – review & editing (equal). **L. Avaldi**: Resources (supporting). **P. Bolognesi**: Data curation (supporting); Investigation (equal). **M. Bonanomi**: Data curation (supporting); Investigation (equal); Validation (equal); Writing – review & editing (equal). **R. Borrego Varillas**: Investigation (supporting). **C. Callegari**: Resources (supporting); Validation (equal); Writing – review & editing (equal). **L. Carlini**: Resources (equal). **J. Chiarinelli**: Resources (supporting); Validation (equal); Writing – review & editing (equal). **E. Ciekalski**: Resources (equal). **M. Coreno**: Investigation (supporting); Validation (equal); Writing – review & editing (equal). **M. Devetta**: Investigation (supporting); Validation (equal); Writing – review & editing (equal). **M. Di Fraia**: Investigation (supporting); Validation (equal); Writing – review & editing (equal). **M. Garavelli**: Conceptualization (equal); Funding acquisition (lead); Validation (equal); Writing – review & editing (equal). **M. Goffe**: Formal analysis (supporting);

Validation (equal); Writing – review & editing (equal). **C. Grazioli**: Investigation (supporting); Validation (equal); Writing – review & editing (equal). **F. Montorsi**: Formal analysis (supporting); Validation (equal); Writing – review & editing (equal). **K.C. Prince**: Investigation (supporting); Validation (equal); Writing – review & editing (equal). **R. Richter**: Investigation (equal); Validation (equal); Writing – review & editing (equal). **F. Segatta**: Formal analysis (equal); Validation (equal); Writing – review & editing (equal). **S. Waldmannstetter**: Resources (equal); Validation (equal); Writing – review & editing (equal). **G. Cerullo**: Conceptualization (equal); Funding acquisition (equal); Validation (equal); Writing – review & editing (equal). **H. Dube**: Resources (lead); Validation (equal); Writing – review & editing (equal). **O. Plekan**: Conceptualization (supporting); Data curation (equal); Investigation (equal); Supervision (supporting); Validation (equal); Writing – review & editing (equal). **D. Faccialà**: Conceptualization (equal); Formal analysis (equal); Funding acquisition (equal); Investigation (equal); Methodology (equal); Project administration (equal); Supervision (equal); Validation (equal); Visualization (equal); Writing – original draft (equal); Writing – review & editing (equal). **C. Vozzi**: Conceptualization (equal); Formal analysis (equal); Funding acquisition (equal); Investigation (equal); Methodology (equal); Project administration (equal); Supervision (equal); Validation (equal); Writing – original draft (equal); Writing – review & editing (equal). **A. Nenov**: Conceptualization (equal); Formal analysis (equal); Funding acquisition (equal); Investigation (equal); Methodology (equal); Project administration (equal); Supervision (equal); Validation (equal); Visualization (equal); Writing – original draft (equal); Writing – review & editing (equal).

DATA AVAILABILITY

The data that support the findings of this study are available within the article and its supplementary material.

REFERENCES

[1] S. Wiedbrauk and H. Dube, Tetrahedron Lett. **56**, 4266–4274 (2015).
[2] M. Guentner, M. Schildhauer, S. Thumser, P. Mayer, D. Stephenson, P. J. Mayer, and H. Dube, Nat. Commun. **6**, 8406 (2015).
[3] A. Gerwien, P. Mayer, and H. Dube, J. Am. Chem. Soc. **140**, 16442 (2018).
[4] A. Gerwien, P. Mayer, and H. Dube, Nat. Commun. **10**, 4449 (2019).
[5] M. Schildhauer, F. Rott, S. Thumser, P. Mayer, R. de Vivie-Riedle, and H. Dube, ChemPhotoChem **3**, 365–371 (2019).
[6] T. Cordes, D. Weinrich, S. Kempa, K. Riesselmann, S. Herre, C. Hoppmann, K. Rück-Braun, and W. Zinth, Chem. Phys. Lett. **428**, 167–173 (2006).
[7] S. Kitzig, M. Thilemann, T. Cordes, and K. Rück-Braun, ChemPhysChem **17**, 1252–1263 (2016).
[8] S. Wiedbrauk, T. Bartelmann, S. Thumser, P. Mayer, and H. Dube, Nat. Commun. **9**, 1456 (2018).
[9] K. Grill and H. Dube, J. Am. Chem. Soc. **142**, 19300 (2020).
[10] N. N. Bach, V. Josef, H. Maid, and H. Dube, Angew. Chem., Int. Ed. **61**, e202201882 (2022).
[11] A. Gerwien, F. Gnannt, P. Mayer, and H. Dube, Nat. Chem. **14**, 670 (2022).
[12] A. Gerwien, M. Schildhauer, S. Thumser, P. Mayer, and H. Dube, Nat. Commun. **9**, 2510 (2018).
[13] T. Fischer, J. Leitner, A. Gerwien, P. Mayer, A. Dreuw, H. Dube, and J. Wachtveitl, J. Am. Chem. Soc. **145**, 14811 (2023).
[14] A. Gerwien, B. Jehle, M. Irmler, P. Mayer, and H. Dube, J. Am. Chem. Soc. **144**, 3029 (2022).
[15] F. F. Graupner, T. T. Herzog, F. Rott, S. Oesterling, R. de Vivie-Riedle, T. Cordes, and W. Zinth, Chem. Phys. **515**, 614–621 (2018).
[16] S. Wiedbrauk, B. Maerz, E. Samoylova, A. Reiner, F. Trommer, P. Mayer, W. Zinth, and H. Dube, J. Am. Chem. Soc. **138**, 12219 (2016).
[17] S. Wiedbrauk, B. Maerz, E. Samoylova, P. Mayer, W. Zinth, and H. Dube, J. Phys. Chem. Lett. **8**, 1585 (2017).
[18] B. Maerz, S. Wiedbrauk, S. Oesterling, E. Samoylova, A. Nenov, P. Mayer, R. de Vivie-Riedle, W. Zinth, and H. Dube, Chem.—Eur. J. **20**, 13984 (2014).
[19] A. Nenov, T. Cordes, T. T. Herzog, W. Zinth, and R. de Vivie-Riedle, J. Phys. Chem. A **114**, 13016–13030 (2010).
[20] F. Montorsi, F. Segatta, A. Nenov, S. Mukamel, and M. Garavelli, J. Chem. Theory Comput. **18**, 1003 (2022).
[21] R. Blyth, R. Delaunay, M. Zitnik, J. Krempasky, R. Krempaska, J. Slezak, K. Prince, R. Richter, M. Vondracek, R. Camilloni *et al.*, J. Electron Spectrosc. Relat. Phenom. **101**, 959 (1999).
[22] T. Hatamoto, M. Matsumoto, X.-J. Liu, K. Ueda, M. Hoshino, K. Nakagawa, T. Tanaka, H. Tanaka, M. Ehara, R. Tamaki, and H. Nakatsuji, J. Electron Spectrosc. Relat. Phenom. **155**, 54–57 (2007).
[23] G. R. Wight and C. E. Brion, J. Electron Spectrosc. Relat. Phenom. **3**, 191–205 (1974).
[24] M. Tronc, G. C. King, and F. H. Read, J. Phys. B: At., Mol. Phys. **12**, 137–157 (1979).
[25] P. Wang, T. X. Carroll, T. D. Thomas, L. J. Sæthre, and K. J. Børve, J. Electron Spectrosc. Relat. Phenom. **251**, 147103 (2021).
[26] T. D. Thomas and R. W. Shaw, J. Electron Spectrosc. Relat. Phenom. **5**, 1081–1094 (1974).
[27] R. N. S. Sodhi and C. E. Brion, J. Electron Spectrosc. Relat. Phenom. **34**, 363–372 (1984).
[28] K. Kimura, S. Katsumata, and Y. Achiba, *Handbook of Hel Photoelectron Spectra of Fundamental Organic Molecules Ionization Energies, Ab Initio Assignments, and Valence Electronic Structure for 200 Molecules* (Japan Scientific Societies Press, 1981).
[29] V. Josef, F. Hampel, and H. Dube, Angew. Chem., Int. Ed. **61**, e202210855 (2022).
[30] L. Carlini, J. Chiarinelli, G. Mattioli, M. C. Castrovilli, V. Valentini, A. De Stefanis, E. M. Bauer, P. Bolognesi, and L. Avaldi, J. Phys. Chem. B **126**, 2968 (2022).
[31] L. Carlini, F. Montorsi, Y. Wu, P. Bolognesi, R. Borrego-Varillas, A. R. Casavola, M. C. Castrovilli, J. Chiarinelli, D. Mocci, F. Vismarra, M. Lucchini, M. Nisoli, S. Mukamel, M. Garavelli, R. Richter, A. Nenov, and L. Avaldi, J. Chem. Phys. **158**, 054201 (2023).
[32] G. Li Manni, I. F. Galván, A. Alavi *et al.*, J. Chem. Theory Comput. **19**, 6933 (2023).
[33] D. Peng and M. Reiher, Theor. Chem. Acc. **131**, 1081 (2012).
[34] J. P. Zobel, P.-O. Widmark, and V. Veryazov, J. Chem. Theory Comput. **16**, 278 (2020).
[35] P. A. Malmqvist, A. Rendell, and B. O. Roos, J. Phys. Chem. **94**, 5477 (1990).
[36] P. Å. Malmqvist, K. Pierloot, A. R. M. Shahi, C. J. Cramer, and L. Gagliardi, J. Chem. Phys. **128**, 204109 (2008).
[37] F. Aquilante, T. Bondo Pedersen, A. Sánchez de Merás, and H. Koch, J. Chem. Phys. **125**, 174101 (2006).
[38] M. G. Delcey, L. K. Sørensen, M. Vacher, R. C. Couto, and M. Lundberg, J. Comput. Chem. **40**, 1789 (2019).
[39] B. N. C. Tenorio, A. Ponzi, S. Coriani, and P. Decleva, Molecules **27**, 1203 (2022).
[40] P.-Å. Malmqvist and B. O. Roos, Chem. Phys. Lett. **155**, 189 (1989).
[41] T. B. Pedersen, F. Aquilante, and R. Lindh, Theor. Chem. Acc. **124**, 1 (2009).
[42] D. Toffoli, A. Guarnaccio, C. Grazioli, T. Zhang, F. Johansson, M. de Simone, M. Coreno, A. Santagata, M. D'Auria, C. Puglia, E. Bernes, M. Stener, and G. Fronzoni, J. Phys. Chem. A **122**, 8745 (2018).
[43] T. Fransson, Y. Harada, N. Kosugi, N. A. Besley, B. Winter, J. J. Rehr, L. G. M. Pettersson, and A. Nilsson, Chem. Rev. **116**, 7551 (2016).

[44]C. Grazioli, O. Baseggio, M. Stener, G. Fronzoni, M. de Simone, M. Coreno, A. Guarnaccio, A. Santagata, and M. D'Auria, J. Chem. Phys. **146**, 054303 (2017).
[45]V. Feyer, O. Plekan, R. Richter, M. Coreno, G. Vall-Llosera, K. C. Prince, A. B. Trofimov, I. L. Zaytseva, T. E. Moskovskaya, E. V. Gromov, and J. Schirmer, J. Phys. Chem. A **113**, 5736 (2009).
[46]O. Plekan, V. Feyer, R. Richter, M. Coreno, G. Vall-Llosera, K. C. Prince, A. B. Trofimov, I. L. Zaytseva, T. E. Moskovskaya, E. V. Gromov, and J. Schirmer, J. Phys. Chem. A **113**, 9376 (2009).
[47]J. Söderström, N. Mårtensson, O. Travnikova, M. Patanen, C. Miron, L. Sæthre, K. Børve, J. Rehr, J. Kas, F. Vila *et al.*, Phys. Rev. Lett. **108**, 193005 (2012).
[48]O. Travnikova, M. Patanen, J. Soderstrom, A. Lindblad, J. J. Kas, F. D. Vila, D. Céolin, T. Marchenko, G. Goldsztejn, R. Guillemin *et al.*, J. Phys. Chem. A **123**, 7619 (2019).
[49]O. Baseggio, D. Toffoli, M. Stener, G. Fronzoni, M. de Simone, C. Grazioli, M. Coreno, A. Guarnaccio, A. Santagata, and M. D'Auria, J. Chem. Phys. **147**, 244301 (2017).
[50]J. V. Ortiz, J. Chem. Phys. **153**, 070902 (2020).
[51]G. Fronzoni, O. Baseggio, M. Stener, W. Hua, G. Tian, Y. Luo, B. Apicella, M. Alfé, M. de Simone, A. Kivimäki, and M. Coreno, J. Chem. Phys. **141**, 044313 (2014).